remote sensing

MDPI

Article

Advanced SAR Interferometric Analysis to Support Geomorphological Interpretation of Slow-Moving Coastal Landslides (Malta, Mediterranean Sea)

Matteo Mantovani [1], Stefano Devoto [2], Daniela Piacentini [3], Mariacristina Prampolini [4,*], Mauro Soldati [4] and Alessandro Pasuto [1]

1 National Research Council of Italy, Research Institute for Geo-Hydrological Protection (CNR-IRPI), Corso Stati Uniti 4, Padova 35127, Italy; matteo.mantovani@irpi.cnr.it (M.M.); alessandro.pasuto@irpi.cnr.it (A.P.)
2 Department of Mathematics and Geosciences, University of Trieste, Via Weiss 2, Trieste 34128, Italy; sdevoto@units.it
3 Department of Pure and Applied Sciences, University of Urbino, Campus Scientifico "E. Mattei", Via Cà le Suore 2/4, Urbino 61029, Italy; daniela.piacentini@uniurb.it
4 Department of Chemical and Geological Sciences, University of Modena and Reggio Emilia, Via Campi 103, Modena 41125, Italy; soldati@unimore.it
* Correspondence: mariacristina.prampolini@unimore.it; Tel.: +39-059-205-8453

Academic Editors: Zhong Lu and Prasad S. Thenkabail
Received: 9 March 2016; Accepted: 18 May 2016; Published: 25 May 2016

Abstract: An advanced SAR interferometric analysis has been combined with a methodology for the automatic classification of radar reflectors phase histories to interpret slope-failure kinematics and trend of displacements of slow-moving landslides. To accomplish this goal, the large dataset of radar images, acquired in more than 20 years by the two European Space Agency (ESA) missions ERS-1/2 and ENVISAT, was exploited. The analysis was performed over the northern sector of Island of Malta (central Mediterranean Sea), where extensive landslides occur. The study was assisted by field surveys and with the analysis of existing thematic maps and landslide inventories. The outcomes allowed definition of a model capable of describing the geomorphological evolution of slow-moving landslides, providing a key for interpreting such phenomena that, due to their slowness, are usually scarcely investigated.

Keywords: SAR interferometry; PSTime; landslides; Malta

1. Introduction

The use of interferometric methods to infer earth surface deformation from satellite-borne synthetic aperture radar has become a regular tool in geoscience since the early 1990s [1]. Generally, sporadic/intermittent movements can be measured, e.g., displacements higher than 1 cm occurring during major earthquakes, deformations in volcanic areas and other kinds of episodic motion [2]. The satellite orbit repetition determines a temporal bracketing as two or more acquisitions are required. Non-episodic motions can be surveyed by combining long series of radar acquisitions thus, it is possible to measure, for example, the rate of subsidence due to mining [3], to ground-water extraction [4] or to slow-moving landsliding [5–7]. The algorithms that are nowadays used to monitor and measure long-term evolution of ground deformation descend from two types of approach: the Short BAseline Subsets (SBAS) proposed by [8], and the PSI (Persistent Scatterer Interferometry) developed by [9].

A technique derived from the latter approach, named Interferometric Point Target Analysis (IPTA) [10], was applied in the overall framework of landslide hazard assessment and management. IPTA was combined with the free-ware PSTime, implemented by [11], to achieve a better comprehension of the geomorphological evolution of extremely slow mass movements. This combined analysis was applied to the north-western portion of the Island of Malta (central Mediterranean Sea), where extensive landslide processes occur [12,13]. Almost 20 years of ERS and ENVISAT acquisitions, stored in the European Space Agency (ESA) archives, were exploited. Analyzing the phase of isolated coherent radar reflectors through time, the evolution of the landslides was tracked and the rate of deformation was measured down to 1–2 mm/year [14]. The interferometric phase histories were then automatically classified according to kinematic classes and trend of movements. The investigation was accompanied by field surveys and with the analysis of existing thematic maps and landslide inventories. The outcomes allowed to define a model capable to describe the evolution of coastal slopes affected by slow-moving landslides, providing a key for interpreting phenomena that are usually scarcely investigated.

2. Study Area

2.1. Geological and Geomorphological Setting

Malta is the main island of the Maltese archipelago, which is located 90 km south of Sicily and 290 km north of Africa. The archipelago rises on the submerged Malta Plateau, through which it is connected with the Hyblean region of Sicily, and constitutes the northern shoulder of the Pantelleria Rift. The Maltese islands are characterized by a Late Oligocene-Miocene stratigraphic sequence made by three carbonatic and one clayey formations. From the oldest to the youngest they are: Lower Coralline Limestone Formation (Fm.), Globigerina Limestone Fm., Blue Clay Fm. and Upper Coralline Limestone Fm. The landscape is shaped by marine action, karst and limited fluvial processes as well as relevant and widespread coastal mass movements.

The study area includes the north-western coast of Malta and is limited southerly by Il-Qarraba peninsula and northerly by Paradise Bay, extending for about 10 km^2 (Figure 1). The structural setting of this portion of the island is characterized by an ENE-WSW oriented *horst* and *graben* system. From a morphological viewpoint, the *grabens* correspond to valleys and lowlands, whereas *horsts* make up plateaus and low-altitude promontories. Along the shoreline, plunging cliffs and rocky coasts alternate with inlets hosting pocket beaches, appreciated by tourists and locals for their pristine beauties [15]. From a geological viewpoint, *horsts* consist of Upper Coralline Limestone Fm., which overlies lowlands or gentle slopes composed by Blue Clay Fm. [16–19]. The superposition of brittle limestone plateaus on plastic-ductile clayey terrains favors slope-failure processes. The anthropic print is less significant than in the southern and eastern coasts, also thanks to the institution of the Il-Majjistral Nature and History Park that allowed protecting the central sector of the study area [20].

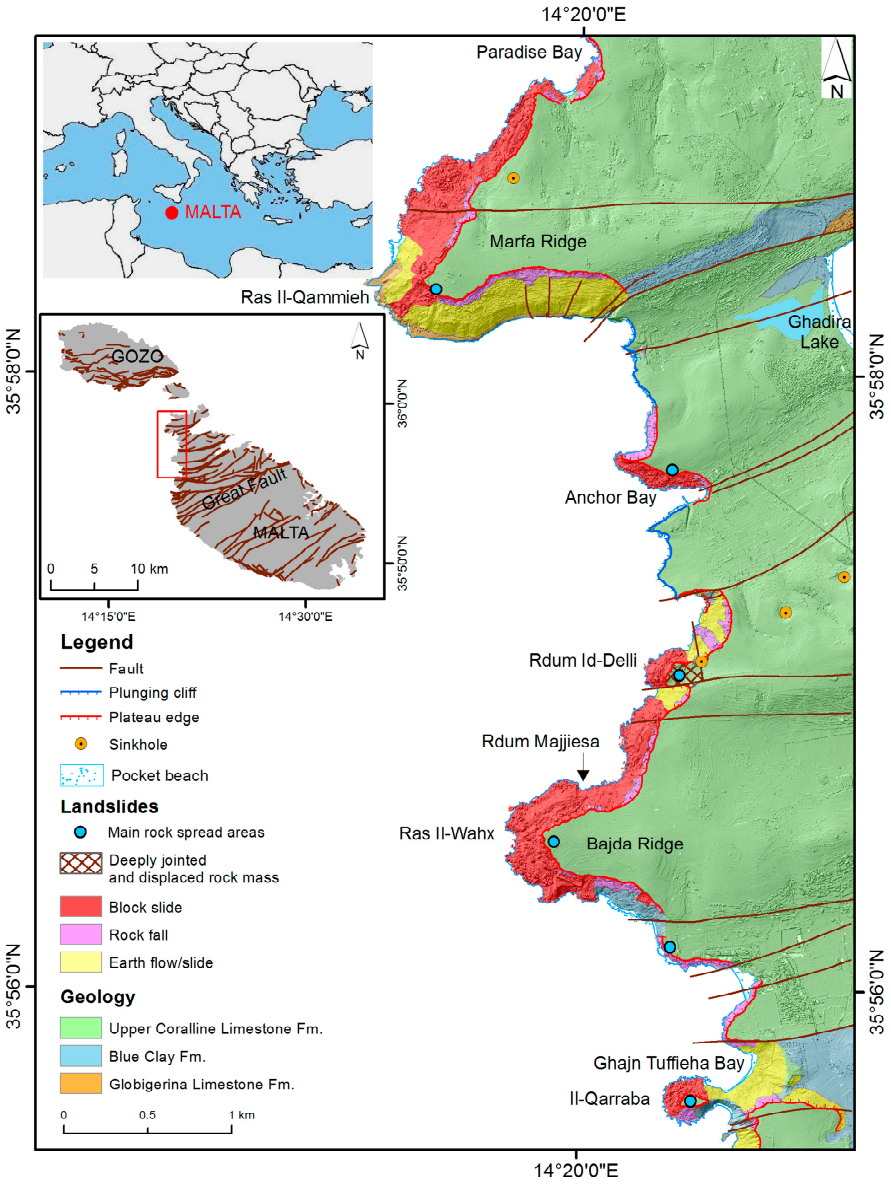

Figure 1. Geological and geomorphological setting of the study area.

2.2. Type and Distribution of Coastal Landslides

Most of the mass movements in the study area are block slides often related to rock spreading and characterized by slow or extremely slow velocities. Rock spreads are witnessed by the presence of several tension cracks located along the edges of the karst plateaus (Figure 2), which can exceed 200 m in horizontal persistence such as in wide sectors of Marfa Ridge plateau (aerial photo 3981 in Figure 2), in the northern portion of Anchor Bay, at Ras Il-Wahx promontory and Il-Qarraba peninsula (aerial photo 4076 in Figure 2). These tension cracks are generated by the different mechanical properties of limestone and the underlying clayey terrains, and favor rainfall infiltration, which feeds the underground karst aquifer. The combination of structural discontinuities and tension cracks, generated and enlarged by the action of rock spreads, isolates limestone pillars or large blocks, which are detached, slowly lowered or toppled from the plateau cliffs. These blocks are abundant and form wide accumulations (named as *rdum* by the locals), which slowly move towards the sea [12,13,21].

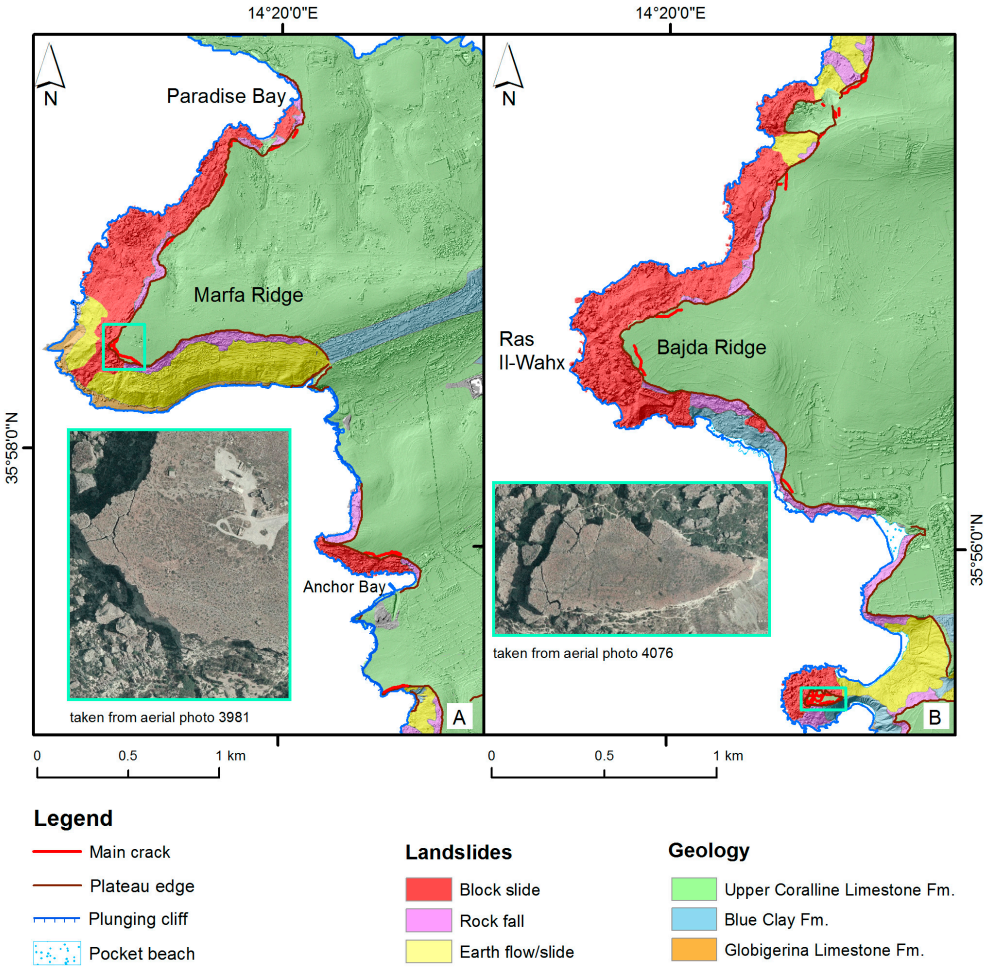

Figure 2. Distributions of the main cracks affecting the plateaus. (**A**) Detail of the northernmost part of the study area; (**B**) detail of the southernmost part of the study area.

3. Materials and Methods

Interferometric Point Target Analysis (IPTA) investigates the temporal and spatial characteristics of the phase backscattered from radar reflectors on the ground to accurately map surface deformation histories, terrain heights and relative atmospheric path delays. Usually, radar reflectors can be found in built environments, since walls and roofs can consistently backscatter the radar signal through time. The displaced limestone blocks over the clayey slopes of the north-western coast of Malta can also be considered suitable reflectors, as it can be noticed by the large amounts of point target candidates detected in the study area.

The processed data include 50 ERS images acquired between 1992 and 2000 and 33 ENVISAT acquisitions covering the period 2004–2009. Details of the processed datasets have been resumed in Tables 1 and 2.

After the co-registration to a single reference image, denoted as Master in the above mentioned tables, the corresponding interferograms were computed. The reference images were chosen among those: (i) acquired near the temporal average of the stack of the processed images, to minimize the temporal decorrelation of interferograms; (ii) provided with an orbit as close as possible to the center of the orbital tube spanned by the stack of the processed images to minimize the spatial decorrelation of interferograms (Figure 3).

Table 1. ERS dataset. Track 494, frame 2889 descending. Images denoted in the NOTES column as noisy are those that have been removed from the final iteration due to the strong presence of atmospheric disturbances. Image denoted with MASTER is the reference images from which all the interferograms have been generated.

No.	Sensor	Date of Acquisition (yyyy-mm-dd)	Orbit Number	Julian Day	Temporal Baseline (days)	Perpen—Dicular Baseline (m)	Notes
1	ERS-1	1992-08-14	5649	2,448,849	−1809	−777	
2	ERS-1	1992-09-18	6150	2,448,884	−1774	436	
3	ERS-1	1992-10-23	6651	2,448,919	−1739	−355	
4	ERS-1	1993-03-12	8655	2,449,059	−1599	−126	
5	ERS-1	1993-05-21	9657	2,449,129	−1529	−121	
6	ERS-1	1993-06-25	10,158	2,449,164	−1494	−86	
7	ERS-1	1993-07-30	10,659	2,449,199	−1459	261	
8	ERS-1	1993-08-10	11,661	2,449,269	−1389	−193	
9	ERS-1	1993-12-17	12,663	2,449,339	−1319	787	
10	ERS-2	1995-11-06	2835	2,450,028	−630	355	
11	ERS-2	1996-04-29	5358	2,450,202	−456	802	
12	ERS-2	1996-08-12	6861	2,450,308	−350	−178	
13	ERS-2	1996-09-16	7362	2450,343	−315	−98	
14	ERS-2	1996-10-21	7863	2,450,378	−280	626	
15	ERS-2	1996-11-25	8364	2,450,413	−245	971	
16	ERS-2	1996-12-30	8865	2,450,448	−210	−30	
17	ERS-2	1997-03-10	9867	2,450,518	−140	28	
18	ERS-2	1997-04-14	10,368	2,450,553	−105	600	
19	ERS-2	1997-07-28	11,871	2,450,658	0	0	Master
20	ERS-2	1997-10-06	12,837	2,450,728	70	386	
21	ERS-2	1997-11-10	13,374	2,450,763	105	−382	
22	ERS-2	1997-12-15	13,875	2,450,798	140	−382	
23	ERS-2	1998-01-19	14,376	2,450,833	175	−447	Noisy
24	ERS-2	1998-02-23	14,877	2,450,868	210	−612	
25	ERS-2	1998-06-08	16,380	2,450,973	315	679	
26	ERS-2	1998-07-13	16,881	2,451,008	350	−574	
27	ERS-2	1998-08-17	17,382	2,451,043	385	−281	
28	ERS-1	1998-09-20	37,556	2,451,077	419	75	
29	ERS-2	1998-09-21	17,883	2,451,078	420	−240	
30	ERS-2	1998-10-26	18,384	2,451,113	455	251	
31	ERS-2	1998-11-30	18,885	2,451,148	490	−127	
32	ERS-2	1999-01-04	19,386	2,451,183	525	−1427	Noisy
33	ERS-2	1999-03-15	20,388	2,451,252	594	130	
34	ERS-2	1999-04-19	20,889	2,451,288	630	513	
35	ERS-2	1999-05-24	21,390	2,451,323	665	121	
36	ERS-2	1999-08-02	22,392	2,451,393	735	2	
37	ERS-2	1999-09-06	22,893	2,451,428	770	−475	
38	ERS-2	1999-10-11	23,394	2,451,463	805	−623	
39	ERS-2	1999-11-15	23,895	2,451,498	840	147	
40	ERS-2	1999-12-20	24,396	2,451,532	874	−178	
41	ERS-2	2000-01-24	24,897	2,451,568	910	33	
42	ERS-2	2000-02-28	25,398	2,451,603	945	−476	
43	ERS-2	2000-04-03	25,899	2,451,638	980	149	
44	ERS-2	2000-05-08	26,400	2,451,673	1015	663	
45	ERS-2	2000-06-12	26,901	2,451,708	1050	−270	
46	ERS-2	2000-07-17	27,402	2,451,743	1085	−478	
47	ERS-2	2000-08-21	27,903	2,451,778	1120	278	
48	ERS-2	2000-09-25	28,404	2,451,813	1155	500	
49	ERS-2	2000-10-30	28,905	2,451,848	1190	73	
50	ERS-2	2000-12-04	29,406	2,451,883	1225	160	

Table 2. ENVISAT dataset. Track 494, frame 2889 descending, swath I2. Images denoted in the NOTES column as noisy are those which have been removed from the final iteration due to the strong presence of atmospheric disturbances. Image denoted with MASTER is the reference images from which all the interferograms have been generated.

No.	Sensor	Date of Acquisition (yyyy-mm-dd)	Orbit Number	Julian Day	Temporal Baseline (days)	Perpen—DICULAR Baseline (m)	Notes
1	ASAR	2003-04-28	6059	2,452,758	−1400	1339	Noisy
2	ASAR	2003-08-11	7562	2,452,863	−1295	−860	Noisy
3	ASAR	2004-02-02	10,067	2,453,038	−1120	665	
4	ASAR	2004-03-08	10,568	2,453,073	−1085	139	
5	ASAR	2004-04-12	11,069	2,453,108	−1050	766	
6	ASAR	2004-05-17	11,570	2,453,143	−1015	−227	
7	ASAR	2004-07-26	12,572	2,453,213	−945	191	
8	ASAR	2004-08-30	13,073	2,453,248	−910	97	Noisy
9	ASAR	2004-10-04	13,574	2,453,283	−875	−103	
10	ASAR	2004-11-08	14,075	2,453,318	−840	−401	
11	ASAR	2004-12-13	14,576	2,453,353	−805	−259	
12	ASAR	2005-01-17	15,077	2,453,388	−770	−349	
13	ASAR	2005-02-21	15,578	2,453,423	−735	−655	
14	ASAR	2005-03-28	16,079	2,453,458	−700	−864	
15	ASAR	2005-08-15	18,083	2,453,598	−560	−198	
16	ASAR	2005-10-24	19,085	2,453,668	−490	349	
17	ASAR	2005-11-28	19,586	2,453,703	−455	−288	
18	ASAR	2006-02-06	20,588	2,453,773	−385	−750	
19	ASAR	2006-03-13	21,089	2,453,808	−350	−66	
20	ASAR	2006-04-17	21,590	2,453,843	−315	−170	
21	ASAR	2006-06-26	22,592	2,453,913	−245	418	
22	ASAR	2006-09-04	23,594	2,453,983	−175	336	Noisy
23	ASAR	2007-01-22	25,598	2,454,123	−35	556	
24	ASAR	2007-02-26	26,099	2,454,158	0	0	Master
25	ASAR	2007-04-02	26,600	2,454,193	35	375	
26	ASAR	2007-06-11	27,602	2,454,263	105	−207	
27	ASAR	2007-08-20	28,604	2,454,333	175	−63	Noisy
28	ASAR	2008-01-07	30,608	2,454,473	315	−474	
29	ASAR	2008-03-17	31,610	2,454,543	385	−205	
30	ASAR	2009-03-02	36,620	2,454,893	735	174	
31	ASAR	2009-04-06	37,121	2,454,928	770	453	
32	ASAR	2009-05-11	37,622	2,454,963	805	−113	
33	ASAR	2009-07-20	38,624	2,455,033	875	33	

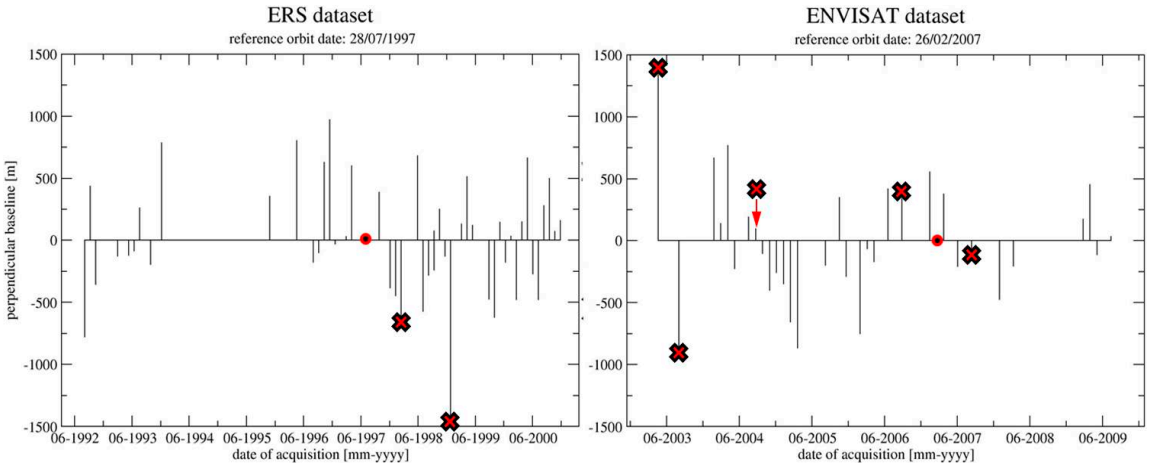

Figure 3. Spatial and temporal baselines of the interferograms. The red spot define the acquisition chosen as reference; red crosses denote noisy interferograms not used in the final processing.

These candidate scenes were then processed with selected images of the stack to generate interferograms characterized by small perpendicular baselines and short time intervals. With a priori knowledge of deformation signal locations and a good coherence, a very flat differential interferogram was interpreted as a clear indication of low atmospheric distortions for both acquisitions and hence in the candidate scene. The interferograms were then subtracted to a synthetic phase, derived from the 3-Arc-Seconds Shuttle Radar Topography Mission (SRTM) Digital Elevation Model (DEM), obtaining 49 ERS and 32 ENVISAT differential interferograms. A Persistent Scatterer (PS) candidates list was compiled based on two detection algorithms implemented in IPTA processing chain. The first one analyzes the spectral properties of individual Single Look Complex (SLC) images and identifies point targets from the spectral behavior and a dominating backscattering. The second exploits large SLC data stacks to detect pixels showing low intensity variability through time. The spatial differences (between pairs of point target candidates) of the differential interferometric phases were analyzed by means of a bi-dimensional regression that takes into account the perpendicular baseline and the time elapsed between two acquisitions. Differences between the measured and modeled phases are related to uncompensated topography, orbital errors, atmospheric path delays, non-linear deformations and noise. Standard deviation of the modeled phase represents a quality index that is used to reject point target candidates that do not meet IPTA requirements. The computation consisted of an iteration process. At the end of every regression, the residuals were inspected, interpreted and filtered out accordingly. In the final phase model, the term related to the displacement was isolated and decomposed in turn as follows:

$$\text{Displacement phase} = (\text{linear deformation phase}) + (\text{non-linear deformation phase}) + (\text{noise}) \quad (1)$$

The freeware PSTime [11] has been recently used for the automatic classification of PS time series. The algorithm, based on a conditional sequence of statistical tests, automatically groups the PS into classes of predefined trends (such as uncorrelated, linear, quadratic, bilinear and discontinuous trend). PSTime was applied to classify the deformation phase histories obtained by the IPTA analysis, in order to investigate the geomorphological evolution of the coastal landslides during the last two decades. Nevertheless, field surveys, previous studies and the analysis of the deformation recorded by a GNSS (Global Navigation Satellite System) monitoring network deployed since 2005 at Anchor Bay and Ghajn Tuffieha Bay [12,13,21] indicated that the kinematic aspects of these landslide do not fit properly the PSTime trend classes. The parameters of the statistical test of PSTime were hence redefined to force the time series in a new customized version of target trends. The deformation recorded at the GNSS benchmarks locations were projected along the sensors LOS (Line of Sight) according to the following formula:

$$d_{LOS} = sin\phi \ (dEcos\theta - dNsin\theta) + dHcos\phi \quad (2)$$

where: d_{LOS} is the deformation along the radar LOS, dE is the deformation measured by the GNSS benchmark in the east coordinate, dN is the deformation measured by the GNSS benchmark in the north coordinate, dH is the deformation measured by the GNSS benchmark in the elevation, ϕ is the look angle of the radar, θ is the azimuth direction.

Deformations along the LOS of the GNSS benchmarks were used as a model to define six new classes (Figure 4a1–f1) that identified rock blocks as:

a. Stable
b. Deforming linearly downhill
c. Deforming linearly uphill
d. Accelerating downhill
e. Decelerating downhill
f. With discontinuous rate and trend

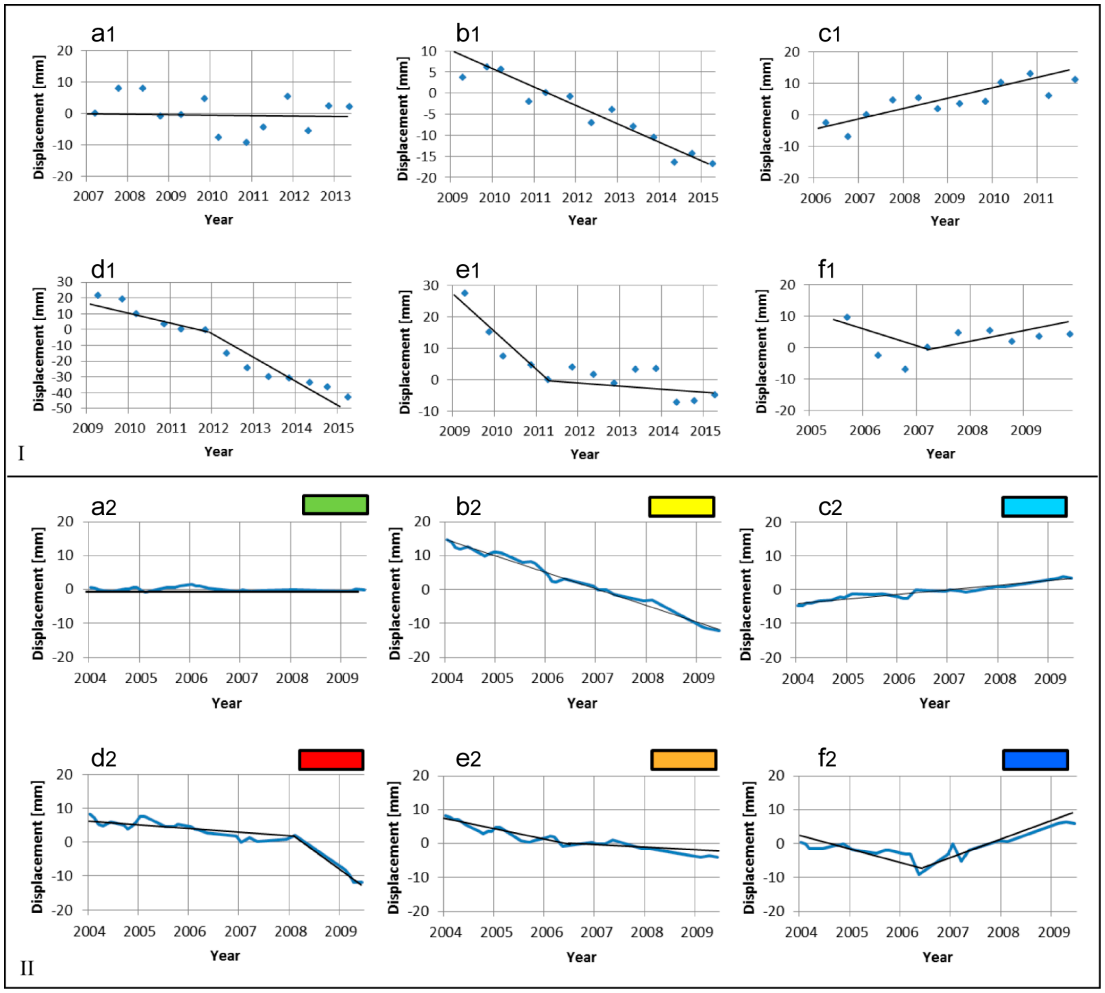

Figure 4. Graphs showing the patterns used to identify the six deformation trend classes used in our model: (**a1**,**a2**) stable; (**b1**,**b2**) deforming linearly downhill; (**c1**,**c2**) deforming linearly uphill; (**d1**,**d2**) accelerating downhill; (**e1**,**e2**) decelerating downhill; (**f1**,**f2**) with discontinuous rate and trend. Sub-figures (**a1**–**f1**) represent the patterns of deformation recorded by GNSS benchmarks and projected along the LOS; sub-figures (**a2**–**f2**) show the time series measured with the interferometric analysis at ENVISAT PS locations.

The good agreement between the new modeled trend classes and the time series actually measured at some representative PS locations can be seen in Figure 4a2–f2. The radar reflectors classified as uncorrelated by the PSTime algorithm and those deforming linearly with a rate included in the interval $(1, -1)$ mm/year were considered stable points in the model.

4. Data Analysis and Results Interpretation

Over the northern part of Malta, 2763 ERS and 6386 ENVISAT persistent scatterers (Figure 5) were identified.

Datasets were processed using the same reference point in order to avoid biased results. Most of the point targets are stable, while deformations are recorded along several sectors of the coast, where slope-failure processes are widespread. PSI processing allowed recognizing active landslides and measure their movement rates, which resulted to be extremely slow, ranging from 1 to 7 mm/year. Furthermore, it is observable that the rate of activity has changed through years. Some sectors show higher rate of deformations in the ERS (1992–2001) acquisitions than in the ENVISAT (2004–2009) and vice-versa. ENVISAT dataset (Figure 5) appears more noisy then ERS because of the lower number

of interferograms processed. Statistical parameters for the assessment of measurement quality are reported in Table 3.

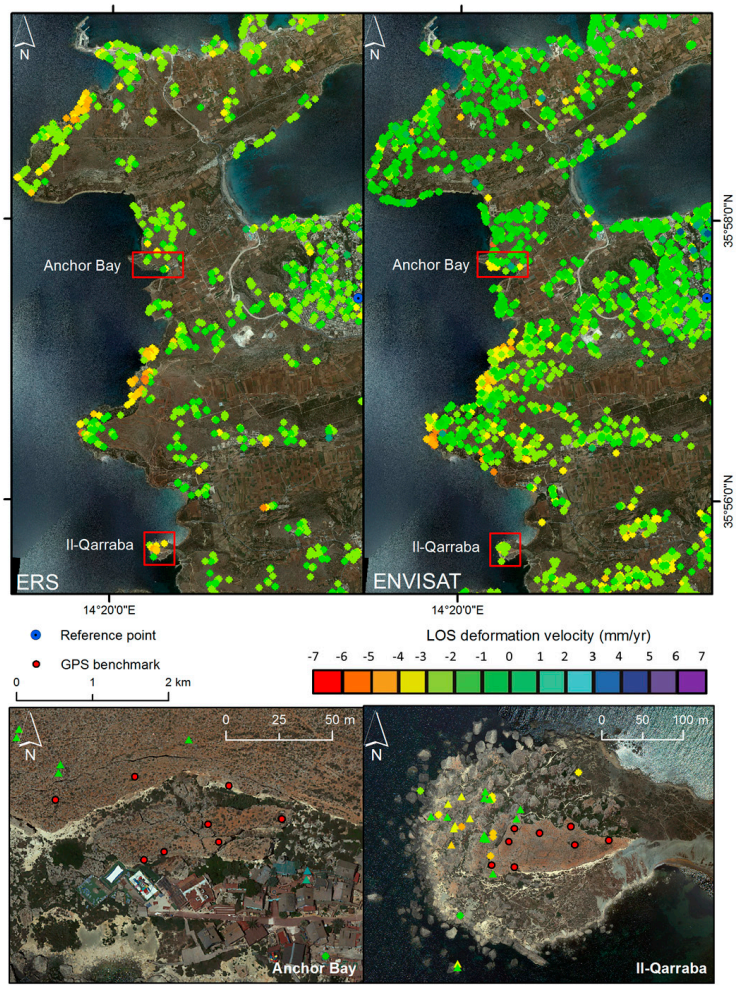

Figure 5. Results of the IPTA analysis performed on the ERS dataset (1999–2000) and ENVISAT dataset (2004–2009). Below the GNSS benchmark location at the site of Anchor Bay and Il-Qarraba.

Table 3. Statistical parameters of the interferometric analysis.

Dataset	Standard Deviation Residual Phase (rad)	Estimated Height Uncertainty (m)	Estimated Deformation Rate Uncertainty (mm/yr)	Stable PS (%)	Deforming PS (%)
ERS	0.616	0.300	0.159	84.80	15.20
ENVISAT	0.627	0.405	0.319	69.95	30.05

In order to evaluate the reliability of the analysis, the deformations recorded by homologous PS (the targets that can be identified in the two datasets) were plotted *versus* time. As it can be noticed from Figure 6, the results appear to be consistent with the expected kinematic behavior of the investigated processes.

Four landslide areas were chosen as test sites for interferometric analysis, based on the presence of a statistically relevant number of targets detected in the two datasets. The chosen areas are the following: (i) western sector of Marfa Ridge; (ii) stretch between Rdum id-Delli and Rdum Majjiesa; (iii) Ras Il-Wahx headland; (iv) peninsula of Il-Qarraba.

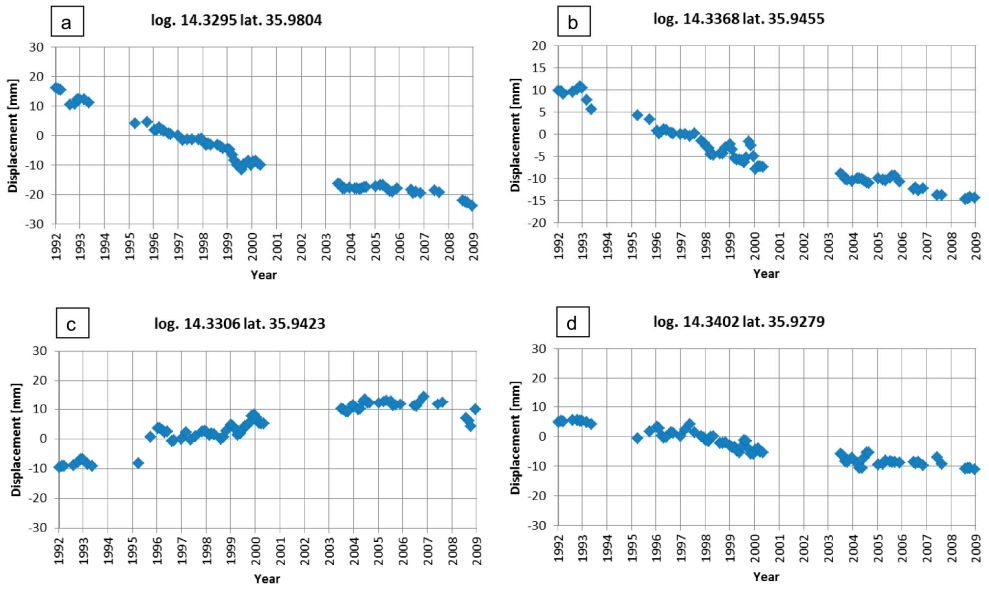

Figure 6. ERS (on the left) and ENVISAT (on the right) time series of four homologous PS located at (**a**) Marfa Ridge; (**b**) Rdum Majjiesa; (**c**) Ras Il-Wahx; (**d**) Il-Qarraba.

4.1. Marfa Ridge Landslides

Marfa Ridge consists of a karst plateau which displays the maximum altitude of the northern coast of Malta (125 m a.s.l.). It is crossed by an E–W oriented system of faults and Globigerina Limestone outcrops at sea level. Towards the sea, the peninsula is characterized by block slides affecting clayey slopes capped by the Upper Coralline Limestone plateau (Figure 7).

Figure 7. Marfa Ridge site seen from the north.

Rock falls and rock topples occur at the edges of the plateau and are favored by rock spreading *cf.* [22]. The histogram in Figure 8 highlights that the majority of ERS PS shows a downhill deformation, while several ENVISAT PS are affected by uplift. Moreover, it can be noticed that the site shows different deformation trends. Thereby, areas characterized by linear subsidence in ERS images and appearing stable in ENVISAT ones are alternated with areas that, in contrast, seem to be stable in ERS dataset and show uplift in ENVISAT acquisitions. A difference in the rate of deformation, can also be noticed from Figure 8, between the northern and the southern sectors, being the former slightly faster. In summary the two dataset allowed us to frame two different stages of an extremely slow deformation process.

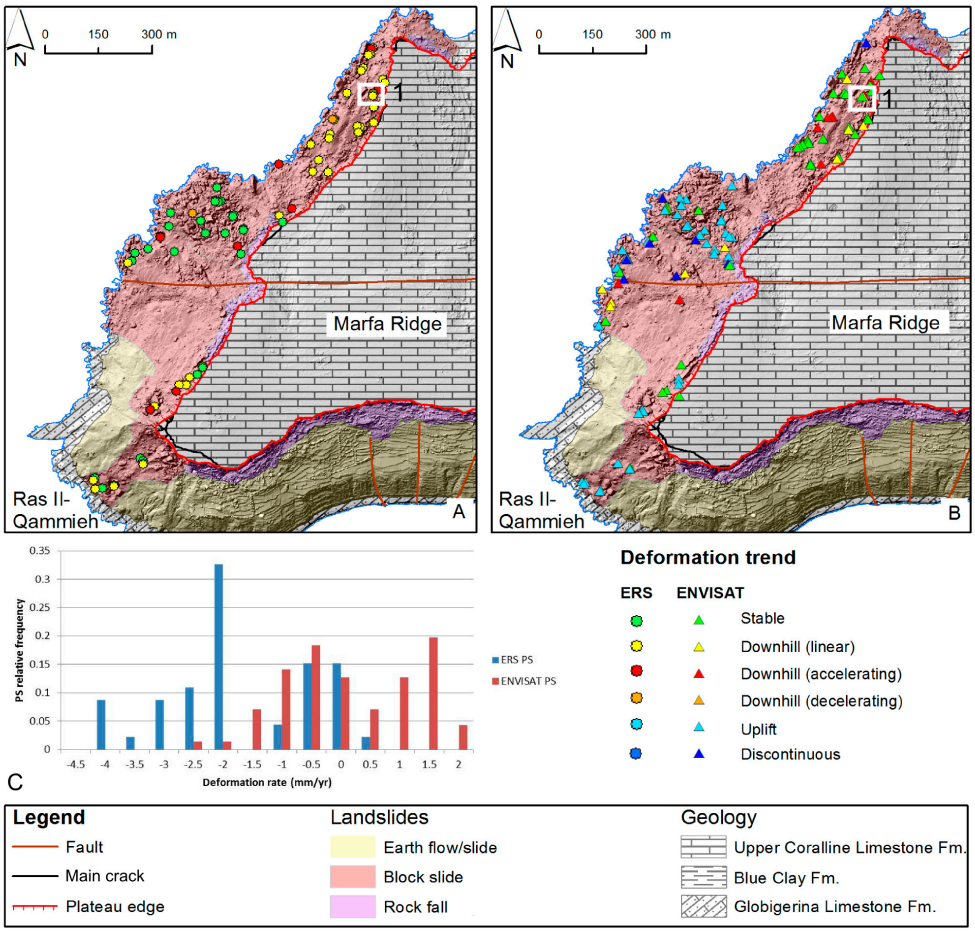

Figure 8. Marfa Ridge landslide map and distribution of the PS, color coded according to the trend classes defined in Figure 4: (**A**) ERS satellite PS deformation trend; (**B**) ENVISAT satellite PS deformation trend; (**C**) Histogram showing the relative frequency of occurrence in each class of movement rate. The white box on the map locates the PS whose time series are reported in Figure 6a.

4.2. Rudm Id-Delli—Rdum Majjiesa Landslides

This site shows different stages of evolution of rock spreading and block sliding: the northernmost part (Rdum id-Delli) is characterized by a limestone plateau from which large portions were isolated and lowered. The latter exhibit a developed network of persistent fractures. At the sea level smaller blocks are abundant. In the southernmost sector (Rdum Majjiesa), rock fall deposits are frequent at the bottom of the plateau edge and are remobilized by block slides (Figure 9).

Figure 9. Rdum id-Delli—Rdum Majjiesa site seen from the south.

PS at Rdum id-Delli block slide show a linear downhill trend through time, except three targets that record a discontinuous rate and trend of deformation, consisting of subsidence followed by uplift. Slight differences in the rate between ERS and ENVISAT dataset can be noticed in the histograms (Figure 10). This stretch of coast shows several accelerating downhill trends.

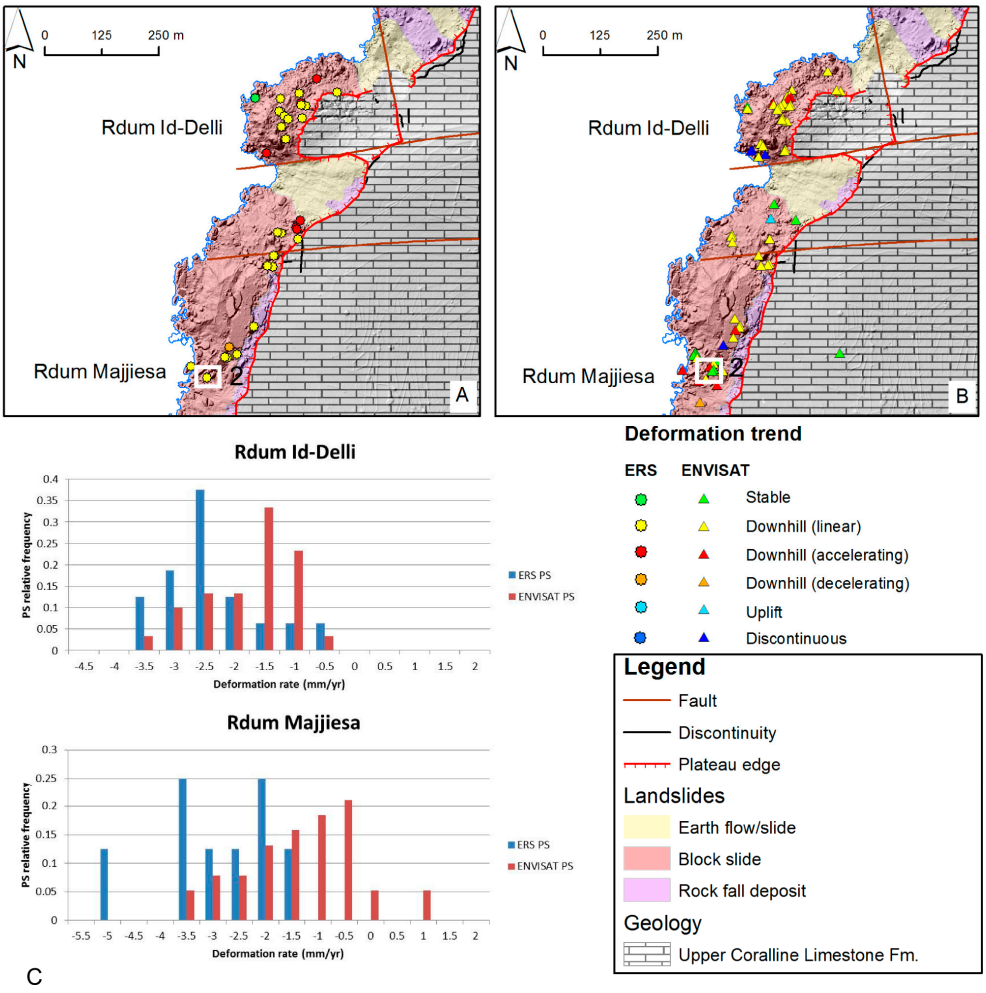

Figure 10. Rdum id-Delli—Rdum Majjiesa landslide map and distribution of the PS, color coded according to the trend classes defined in Figure 4: (**A**) ERS satellite PS deformation trend; (**B**) ENVISAT satellite PS deformation trend; (**C**) Histogram showing the relative frequency of occurrence in each class of movement rate. Blue bars are ERS PS, red are ENVISAT. The white box on the maps locate the PS whose time series are reported in Figure 6b.

4.3. Ras Il-Wahx Landslides

The western sector of the 100 m-high Ras Il-Wahx promontory shows spectacular landslides (Figure 11). Rock spreading affects a deeply jointed area extending inland up to 70 m from the cliff edge. The headland is surrounded by block slide accumulations, which consist of tens of piled-up blocks sometimes of relevant volume. These are partially sunk in the clayey terrains and rotated backward.

According to interferometric analysis this site shows the highest deformation rates of the entire north-western coast. Moreover, this is the only sector of the coast where the rate of deformation has increased through time (see histogram in Figure 12), despite a small cluster of blocks in the northern part of the promontory that reached stability (ENVISAT dataset) after an evolution characterized by discontinuous deformation rate and trend (ERS dataset).

Figure 11. Ras Il-Wahx site seen from the south.

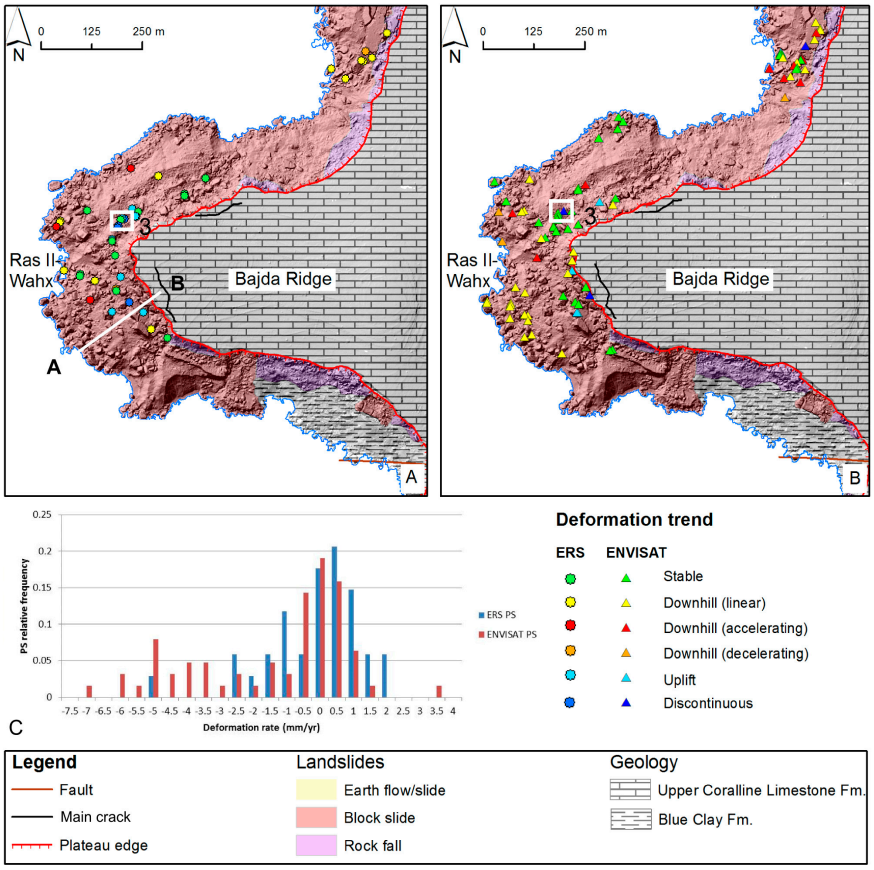

Figure 12. Ras Il-Wahx landslide map and distribution of the PS, color coded according to the trend classes defined in Figure 4: (**A**) ERS satellite PS deformation trend; (**B**) ENVISAT satellite PS deformation trend; (**C**) Histogram showing the relative frequency of occurrence in each class of movement rate. The white box on the map locates the PS whose time series are reported in Figure 6c. The white line defines the cross section of Figure 13.

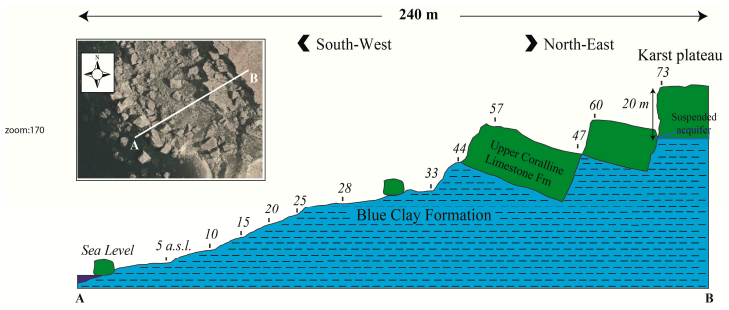

Figure 13. SW-NE geological section of Ras Il-Wahx site (Figure 12) showing block slides phenomena.

4.4. Il-Qarraba Landslides

A peculiar landform of Malta is the head-shaped peninsula of Il-Qarraba, which is connected to inland through a narrow isthmus of clayey and marly terrains [17]. The latter are overlain in the central part of the peninsula by a flat limestone slab, characterized by 10 m-high cliffs. The western and northern portions of the limestone slab are affected by rock spreads evolving into block slides characterized by the presence of huge blocks. The limestone blocks move towards the sea and are dominant in the western and northern sector of the peninsula (Figure 14). Both the ERS and ENVISAT datasets show the same trend of deformation (Figure 15): the blocks are either stable or linearly subsiding and no uplifting is recorded, except for few PS.

Figure 14. Il-Qarraba peninsula seen from the north.

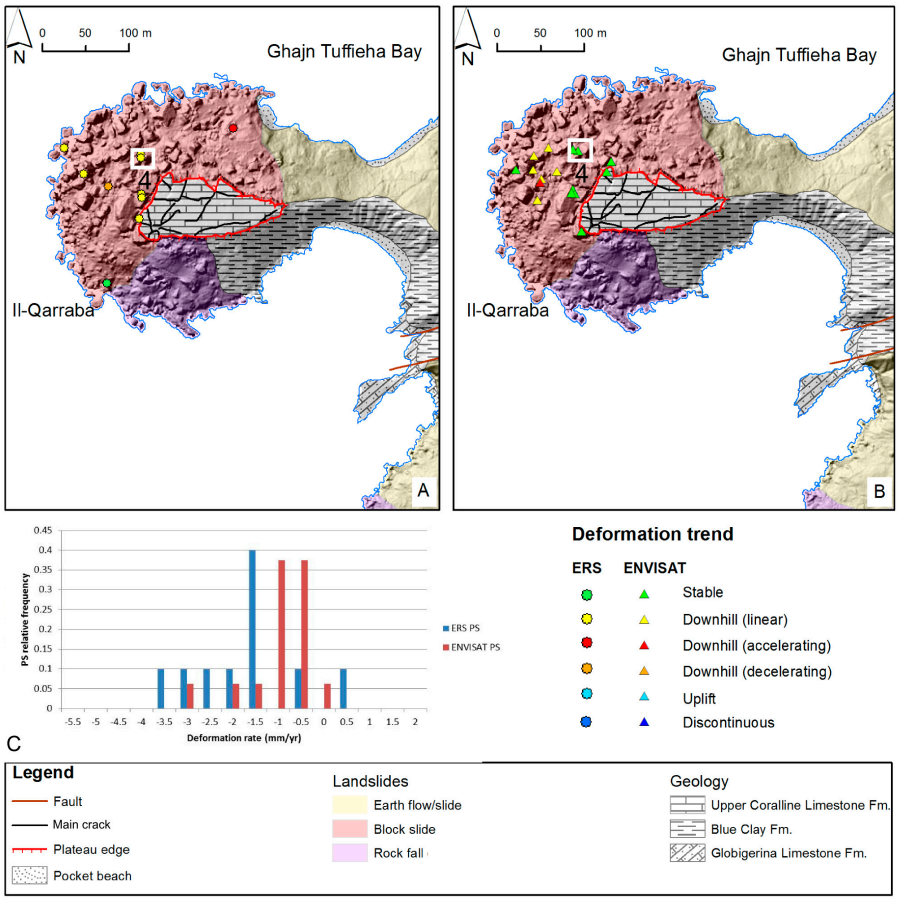

Figure 15. Il-Qarraba landslide map and distribution of the PS, color coded according to the trend classes defined in Figure 4: (**A**) ERS satellite PS deformation trend; (**B**) ENVISAT satellite PS deformation trend; (**C**) Histogram showing the relative frequency of occurrence in each class of movement rate. The white box on the map locates the PS whose time series are reported in Figure 6d.

5. Discussion

The analysis of the results cannot be separated from a brief discussion on the constraints of the technique employed to measure deformations. Considering that there are no substantial differences in terms of wavelength and acquisition geometry between the synthetic radar mounted on board of ERS and ENVISAT satellites and that the images are acquired from the same track, it can be assumed that the sensitivity to deformations is the same in the two datasets. The fact that block slide movement direction is mainly E-W oriented makes interferometric measurement very effective [23]. Taking into account that Malta was framed from a descending orbit, the expected downhill displacement of the limestone blocks resulted in an increment of the LOS distance. In contrast the shortening of the LOS distance, that in the previous chapters was simply defined as uplift, can be interpreted as a back-tilting of the limestone blocks towards the sensor favored by the swelling of the clayey deposits. The evolution of the landslides which characterize the north-western coast of Malta is in agreement with the model proposed by [21,22,24], according to which the deformation process is composed by the following three phases: (i) rock spreading affecting the intensely jointed limestone cap; (ii) progressive detachment of limestone blocks of large size from the plateau; (iii) tilting and sliding of the blocks above the underlying clays which deform visco-plastically. Within this framework, rock falls and earth flows/slides represent shallow evidence of a deeper movement involving the entire slope from the plateau to the coastline. Lateral spreading also favors the development of bulges in the clays at the foot of the cliffs because of the overburden [25]. Moreover, the results here obtained properly fit with the model proposed by [21], that applied a multidisciplinary approach by means of geomorphological and geophysical surveys and *in situ* monitoring activities at Anchor Bay site.

IPTA analysis coupled with PSTime algorithm allowed to detect and discriminate six different phase variation patterns that can be associated to the above mentioned evolutionary model (Figure 13).

These phase trends can be interpreted from a geomorphological viewpoint as follows:

1. *Stable area.* No significant deformation trend can be detected by the interferometric analysis. The majority of stable PS can be found in correspondence of wide block slide deposits or over the less jointed portions of plateaus. It is likely that the stability of the latter can be related to the limited thickness of the limestone slabs or to the presence of extensive network of joints that do not favor the presence of a karst aquifer. These types of settings occur at Il-Qarraba for which the interferometric results confirm the above mentioned hypothesis.
2. *Downhill-moving area.* A significant increment in LOS distance between the target and the sensor can be detected. The associated deformation trend can be interpolated linearly and can be constant through time or discontinuous (*i.e.*, accelerating or decelerating). The PS showing this behavior were interpreted as blocks detached from the plateau that began to move downward towards the sea. The deformation process may be ascribable to the presence of a slip surface. This kind of movement is more common in the upper part of steep slopes as in the area of Rdum id-Delli and Rdum Majjiesa. Again the interferometric results appear consistent with this geomorphological interpretation.
3. *Discontinuous-moving area.* The seaward translation of the blocks on the surface is irregular. When the steepness of the slope decreases or the slip surface progressively becomes sub-horizontal, the blocks might come to a temporary rest. The consequent uplift measured in terms of reduction of the LOS is likely to be associated to a backward tilting of the blocks towards the plateau favored by the bulging and expansion of the underlying clay. This style of deformation is evident at Marfa Ridge where blocks that slide towards the sea, according to the ERS dataset, subsequently showed a back-tilting in the interferometric analysis performed using ENVISAT images. On the other hand, according to PS measurements on ERS dataset, at Ras Il-Whax blocks first show a discontinuous deformation trend and then appear to be stable or to re-start their descent along the slope.

4. *Uplift-moving area.* It is the natural evolution of the discontinuous trend, as a matter of fact it is frequently observed around cluster of blocks characterized by this type of deformation as can be clearly noted in Figures 7 and 11. This behavior is also favored by the bulging and the expansion of the underlying clay.

It is likely that the main factors controlling the style and rate of the deformations are the weight of the limestone plateaus; the relative ratios of limestone plateau and clayey terrains thickness; and the undermining at the toe of the cliff. Where the limestone caps have considerable thickness and the clayey terrains outcrops at sea level, the displacement rates are higher: perfect examples are Ras Il-Wahx site and the coast comprised between Rdum id-Delli and Rdum Majjiesa where 20 m-thick of limestone cap can be found, which is almost the double of the thickness recorded at Il-Qarraba. Another proof of this hypothesis is the case of Marfa Ridge: on the northernmost sector of the ridge, the blocks show higher rates of movement compared to the south. Again, a considerable thickness of the limestone plateau (17 m) can be found along with the outcropping of Blue Clays at sea level. This setting is not preserved in the southernmost part, where the Globigerina limestone appears along the coastline. The process of undermining is the direct consequence of marine water action and the presence of an aquifer inside the limestone slab that favors the occurrence of springs at the contact between limestone and clay. This process can be found along the stretch of coast between Rdum id-Delli and Ras Il-Wahx and where relatively high rate of displacements have been recorded from the interferometric analysis.

6. Conclusions

The analysis of long-term evolution of widespread slow-moving landslides is an expensive and time-consuming task to achieve using traditional monitoring techniques. Advanced SAR interferometric analyzes represent nowadays the only suitable methodology, even by virtue of the fact of being able to exploit nearly 20 years of data. Interferometric methods have been often used to measure surface displacements caused by mass movements, but in this study IPTA processing and a modified version of PSTime algorithm were coupled in order to provide more relevant information. These outcomes assisted in the geomorphological interpretation of slow-moving landslides, which are seldom investigated with such detailed accuracy. From the interferometric phase, information allowing to define a model of the Maltese coastal landslides, congruent to field observations and GNSS measurements, were extracted. The mechanism of evolution was inferred and reliable measurements of the rate and trend of deformation were provided. The importance of the results achieved is evident assuming that all the information collected from the interferometric analysis is crucial for an effective landslide hazard assessment [26]. The combined methodology used in this study shows the potential for being extended to other areas affected by slow-moving landslides and characterized by similar geological settings. Further developments of this research will include the collection and analysis of the new ESA mission Sentinel-1 up-to-date datasets.

Acknowledgments: The authors acknowledge European Space Agency for providing ERS and ENVISAT radar images (C1P.7044). The research is part of a project of the Euro-Mediterranean Center on Insular Coastal Dynamics (ICoD) funded by the EUR-OPA Major Hazards Agreement of the Council of Europe (2013–2015). The paper is also part of the PRIN 2010-11 MIUR Project on the "Dynamics of morphoclimatic systems as a response of global changes and induced geomorphological risks" (coordinator: C. Baroni; research unit responsible: M. Soldati).

Author Contributions: Matteo Mantovani processed the datasets and performed the interferometric analysis. Stefano Devoto, Daniela Piacentini and Mariacristina Prampolini performed the field surveys and contributed in the formulation of the geomorphological model of landslides evolution. Alessandro Pasuto and Mauro Soldati led the research and assisted in the result interpretation. All authors contributed to paper writing and revision.

Conflicts of Interest: The authors declare no conflict of interest.

Abbreviations

The following abbreviations are used in this manuscript:

SBAS	Short Baseline Subsets
PSI	Persistent Scatterer Interferometry
IPTA	Interferometric Point Target Analysis
ESA	European Space Agency
SRTM	Second Shuttle Radar Topography Mission
DEM	Digital Elevation Model
PS	Persistent Scatterer
SLC	Single Look Complex
LOS	Line of Sight
GNSS	Global Navigation Satellite System

References

1. Bamler, R.; Hartl, P. Synthetic aperture radar interferometry. *Inverse Probl.* **1998**, *14*. [CrossRef]
2. Hooper, A.; Zebker, H.; Segall, P.; Kampes, B. A new method for measuring deformation on volcanoes and other natural terrains using InSAR persistent scatterers. *Geophys. Res. Lett.* **2004**, *31*. [CrossRef]
3. Carnec, C.; Delacourt, C. Three years of mining subsidence monitored by SAR interferometry, near Gardanne, France. *J. Appl. Geophys.* **2000**, *43*, 43–54. [CrossRef]
4. Tomás, R.; Márquez, Y.; Lopez-Sanchez, J.M.; Delgado, J.; Blanco, P.; Mallorquí, J.J.; Martinez, M.; Herrera, G.; Mulas, J. Mapping ground subsidence induced by aquifer overexploitation using advanced Differential SAR Interferometry: Vega Media of the Segura River (SE Spain) case study. *Remote Sens. Environ.* **2005**, *98*, 269–283. [CrossRef]
5. Berardino, P.; Costantini, M.; Franceschetti, G.; Iodice, A.; Pietranera, L.; Rizzo, V. Use of differential SAR interferometry in monitoring and modelling large slope instability at Maratea (Basilicata, Italy). *Eng. Geol.* **2003**, *68*, 31–51. [CrossRef]
6. Calo, F.; Ardizzone, F.; Castaldo, R.; Lollino, P.; Tizzani, P.; Guzzetti, F.; Manunta, M. Enhanced landslide investigations through advanced DInSAR techniques: The Ivancich case study, Assisi, Italy. *Remote Sens. Environ.* **2014**, *142*, 69–82. [CrossRef]
7. Gigli, G.; Frodella, W.; Mugnai, F.; Tapete, D.; Cigna, F.; Fanti, R.; Intrieri, E.; Lombardi, L. Instability mechanisms affecting cultural heritage sites in the Maltese Archipelago. *Nat. Hazards Earth Syst. Sci.* **2012**, *12*, 1883–1903. [CrossRef]
8. Berardino, P.; Fornaro, G.; Lanari, R.; Sansosti, E. A new algorithm for surface deformation monitoring based on small baseline differential SAR interferograms. *IEEE Trans. Geosci. Remote Sens.* **2002**, *40*, 2375–2383. [CrossRef]
9. Ferretti, A.; Prati, C.; Rocca, F. Permanent scatterers in SAR interferometry. *IEEE Trans. Geosci. Remote Sens.* **2001**, *39*, 8–20. [CrossRef]
10. Werner, C.; Wegmuller, U.; Strozzi, T.; Wiesmann, A. Interferometric point target analysis for deformation mapping. In Proceedings of the IEEE International 2003 Geoscience and Remote Sensing Symposium, Toulouse, France, 21–25 July 2003; pp. 4362–4364.
11. Berti, M.; Corsini, A.; Franceschini, S.; Iannacone, J.P. Automated classification of Persistent Scatterers Interferometry time series. *Nat. Hazards. Earth Syst. Sci.* **2013**, *13*, 1945–1958. [CrossRef]
12. Magri, O.; Mantovani, M.; Pasuto, A.; Soldati, M. Geomorphological investigation and monitoring of lateral spreading along the north-west coast of Malta. *Geogr. Fisica Din. Quat.* **2008**, *31*, 171–180.
13. Devoto, S.; Biolchi, S.; Bruschi, V.M.; Díez, A.G.; Mantovani, M.; Pasuto, A.; Piacentini, D.; Schembri, J.A.; Soldati, M. Landslides along the north-west coast of the Island of Malta. In *Landslide Science and Practice*; Margottini, C., Canuti, P., Sassa, K., Eds.; Springer: Berlin, Germany; Heidelberg, Germany, 2013; Volume 1, pp. 57–63.
14. Casu, F.; Manzo, M.; Lanari, R. A quantitative assessment of the SBAS algorithm performance for the surface deformation retrieval from DInSAR data. *Remote Sens. Environ.* **2006**, *102*, 195–210. [CrossRef]
15. Biolchi, S.; Furlani, S.; Devoto, S.; Gauci, R.; Castaldini, D.; Soldati, M. Geomorphological identification, classification and spatial distribution of coastal landforms of Malta (Mediterranean Sea). *J. Maps* **2016**, *12*, 87–99. [CrossRef]

16. Alexander, D. A review of the physical geography of Malta and its significance for tectonic geomorphology. *Quat. Sci. Rev.* **1988**, *7*, 41–53. [CrossRef]
17. Dykes, A.P. Mass movements and conservation management in Malta. *J. Environ. Manag.* **2002**, *66*, 77–89. [CrossRef]
18. Pedley, M.; Clarke, M.H. *Limestone Isles in a Crystal Sea: The Geology of the Maltese Islands*; Publishers Enterprises Group: San Gwann, Malta, 2002.
19. Devoto, S.; Biolchi, S.; Bruschi, V.M.; Furlani, S.; Mantovani, M.; Piacentini, D.; Pasuto, A.; Soldati, M. Geomorphological map of the NW Coast of the Island of Malta (Mediterranean Sea). *J. Maps* **2012**, *8*, 33–40. [CrossRef]
20. Coratza, P.; Bruschi, V.M.; Piacentini, D.; Saliba, D.; Soldati, M. Recognition and assessment of geomorphosites in Malta at the Il-Majjistral Nature and History Park. *Geoheritage* **2011**, *3*, 175–185. [CrossRef]
21. Mantovani, M.; Devoto, S.; Forte, E.; Mocnik, A.; Pasuto, A.; Piacentini, D.; Soldati, M. A multidisciplinary approach for rock spreading and block sliding investigation in the north-western coast of Malta. *Landslides* **2013**, *10*, 611–622. [CrossRef]
22. Pasuto, A.; Soldati, M. Lateral Spreading. In *Treatise on Geomorphology*; Shroder, J.F., Ed.; Academic Press: San Diego, CA, USA, 2013; Volume 7, pp. 239–248.
23. Colesanti, C.; Wasowski, J. Investigating landslides with space-borne Synthetic Aperture Radar (SAR) interferometry. *Eng. Geol.* **2006**, *88*, 173–199. [CrossRef]
24. Conti, S.; Tosatti, G. Tectonic *vs.* gravitational processes affecting Ligurian and Epiligurian units in the Marecchia valley (northern Apennines). *Mem. Sci. Geol.* **1996**, *48*, 107–142.
25. Brunsden, D. The case of the missing ductile layer. *J. Geol. Soc. China* **1996**, *39*, 535–556.
26. Piacentini, D.; Devoto, S.; Mantovani, M.; Pasuto, A.; Prampolini, M.; Soldati, M. Landslide susceptibility modeling assisted by Persistent Scatterers Interferometry (PSI): An example from the northwestern coast of Malta. *Nat. Hazards* **2015**, *78*, 681–697. [CrossRef]